Assessment of tumor redox status through (*S*)-4-(3-[^{18}F]fluoropropyl)-L-glutamic acid positron emission tomography imaging of system x_c^- activity

Patrick N. McCormick[1], Hannah E. Greenwood[1], Matthias Glaser[2], Oliver D.K. Maddocks[3], Thibault Gendron[2], Kerstin Sander[2], Gayatri Gowrishankar[4], Aileen Hoehne[4], Tong Zhang[3], Adam J. Shuhendler[4], David Y. Lewis[4], Mathias Berndt[5], Norman Koglin[5], Mark F. Lythgoe[1], Sanjiv S. Gambhir[4,6], Erik Årstad[2], Timothy H. Witney[1,*]

[1] Centre for Advanced Biomedical Imaging, Division of Medicine, University College London, London, UK

[2] Institute of Nuclear Medicine and Department of Chemistry, University College London, London, UK

[3] Wolfson Wohl Cancer Research Centre, Institute of Cancer Sciences, University of Glasgow, Glasgow, UK

[4] Department of Radiology, Molecular Imaging Program, Stanford University, Palo Alto, CA, USA

[5] Life Molecular Imaging GmbH, 13353 Berlin, Germany

[6] Department of Bioengineering, Department of Materials Science and Engineering, Bio-X, Stanford University, Palo Alto, USA

* Corresponding Author: Timothy H. Witney (tim.witney@kcl.ac.uk); Current address: School of Biomedical Engineering and Imaging Sciences, Department of Imaging Chemistry and Biology, King's College London, St Thomas' Hospital, London SE1 7EH

Running Title: Imaging tumor redox status with [^{18}F]FSPG PET

Keywords: [^{18}F]FSPG, positron emission tomography, system x_c^-, cystine, glutathione

Declaration of interests: Timothy Witney and Sanjiv Sam Gambhir received research funding from Life Molecular Imaging GmbH, who own the patent for [^{18}F]FSPG. Timothy Witney is a consultant for CellSight Technologies Inc. Norman Koglin and Mathias Berndt are employees of Life Molecular Imaging and coinventors of [^{18}F]FSPG. Erik Årstad received commercial funding from Mallinckrodt Pharmaceuticals and Oliver Maddocks contributed to CRUK Cancer Research Technology filing of UK Patent Application no. 1609441.9. All other authors have no conflicts of interest to declare.

Word Count: 5,082

Figure Count: 5

ABSTRACT

The cell's endogenous antioxidant system is vital to maintenance of redox homeostasis. Despite its central role in normal and pathophysiology, no non-invasive tools exist to measure this system in patients. The cystine/glutamate antiporter system x_c^- maintains the balance between intracellular reactive oxygen species and antioxidant production through the provision of cystine, a key precursor in glutathione biosynthesis. Here we show that tumor cell retention of a system x_c^--specific positron emission tomography radiotracer, (*S*)-4-(3-[^{18}F]fluoropropyl)-L-glutamic acid ([^{18}F]FSPG), decreases in proportion to levels of oxidative stress following treatment with a range of redox-active compounds. The decrease in [^{18}F]FSPG retention correlated with a depletion of intracellular cystine resulting from increased de novo glutathione biosynthesis, shown through [U-$^{13}C_6$, U-$^{15}N_2$]cystine isotopic tracing. *In vivo*, treatment with the chemotherapeutic doxorubicin decreased [^{18}F]FSPG tumor uptake in a mouse model of ovarian cancer, coinciding with markers of oxidative stress but preceding tumor shrinkage and decreased glucose utilization. Having already been used in pilot clinical trials, [^{18}F]FSPG PET could be rapidly translated to the clinic as an early redox indicator of tumor response to treatment.

INTRODUCTION

Mammalian cells have developed an exquisite system of biochemical processes with which to maintain redox homeostasis. The overall purpose of this system is to prevent damage from unregulated redox reactions. For example, harmful reactive oxygen species (ROS) generated during oxidative phosphorylation are buffered by the activity of multiple enzymes including superoxide dismutase, catalase, and glutathione peroxidase, which convert ROS to increasingly benign products. Other toxic redox-active compounds include exogenous electrophiles, which can be neutralized by an array of intracellular antioxidants, such as glutathione (GSH) and thioredoxin (Trx), along with associated oxidoreductase enzymes. While these mechanisms are usually sufficient to maintain redox homeostasis, prolonged or elevated exposure to ROS or exogenous electrophiles can result in damage to DNA, proteins and cell membranes (reviewed in (1)). The consequences of redox dysregulation – cumulatively referred to as oxidative stress – play an important role in a myriad of diseases, including cancer (2, 3), arthritis (4), cardiovascular disease (5), Alzheimer's disease and Parkinson's disease (6).

Cancer cells reprogram their metabolism to meet the energetic and biosynthetic demands accompanying elevated rates of replication (7). A common consequence of this metabolic adaptation is an elevation in ROS (8). To avoid the cytotoxicity associated with high ROS levels, cancer cells can adapt by upregulating key antioxidant molecules such as GSH and Trx (9). Additionally, many chemotherapeutic agents are known to produce oxidative stress, as evidenced by elevation of lipid peroxidation products, diminished radical-trapping capacity of blood plasma, decreased plasma levels of antioxidants such as vitamin E, vitamin C, and β-carotene, and the

marked depletion of tissue GSH (10-12). Not surprisingly, acquired resistance to chemotherapeutics is often associated with increased levels of antioxidants (e.g. GSH, Trx) and associated oxidoreductases (e.g. GSH peroxidase and γ-glutamyl transpeptidase) (9, 13).

Given the importance of redox processes in cancer, a sensitive and non-invasive measure of cellular redox status would enable a greater understanding of mechanisms that drive disease progression, chemotherapy response and resistance. A number of *in vivo* redox imaging approaches are currently under preclinical development, including ROS-sensitive PET radiotracers (14-16), the cystine analog [^{18}F]FASu (17, 18), redox-sensitive MRI contrast agents (19), and hyperpolarized magnetic resonance spectroscopy imaging (MRSI) techniques (20, 21). The validation of these techniques, however, are at a relatively preliminary stage and none have been translated to human use. The lack of translational redox imaging techniques represents a major gap in the arsenal of human imaging methods. Here, we use the PET radiotracer (*S*)-4-(3-[^{18}F]fluoropropyl)-L-glutamic acid ([^{18}F]FSPG) as an *in vivo* probe of intracellular redox status. In patients, [^{18}F]FSPG PET has been used to image a range of malignancies, including lung, liver and brain cancers (22-25). However, the link between [^{18}F]FSPG uptake and tumor redox status has not been previously investigated.

[^{18}F]FSPG enters the cell via the system x_c^- membrane transporter (26), a heterodimeric transporter comprising the functional transporter, xCT/SLC7A11, and SLC3A2, a membrane protein common to several amino acid transporters. Physiologically, system x_c^- functions as a cystine/glutamate antiporter, allowing extracellular cystine, the dimeric form of cysteine, to be taken up in exchange for intracellular glutamate (27). Within the cell, cystine is reduced to cysteine (28), the rate-

limiting substrate in the biosynthesis of GSH (29), the cell's most abundant small molecule antioxidant (30). System x_c^--derived cystine represents one of the primary sources of intracellular cysteine, particularly under conditions of oxidative stress when system x_c^- expression and cysteine demand are increased (31). High levels of system x_c^- expression result in increased cystine influx (32) and GSH biosynthesis (33), processes which utilize intracellular glutamate as an exchange partner and biosynthetic precursor, respectively. This x_c^-/cystine-mediated shunting of glutamate away from anaplerotic reactions is thought to be the driving force behind reduced glutamine dependence observed in tumors when compared to cells grown in culture (32).

Specific uptake via system x_c^- transport places [^{18}F]FSPG at a central position within the cell's antioxidant system. Accordingly, we hypothesized that [^{18}F]FSPG PET would provide a useful tool for *in vivo* imaging of cellular redox status. Moreover, the fact that [^{18}F]FSPG has already been used in pilot clinical trials provides the possibility for its rapid translation to human redox imaging. In this study we characterize changes in [^{18}F]FSPG retention in response to oxidant and antioxidant treatments. Using a metabolomics approach, we then address the molecular mechanisms underlying the observed changes in [^{18}F]FSPG uptake. Finally, we evaluate the utility of [^{18}F]FSPG for *in vivo* imaging of tumor redox status in a mouse model of ovarian cancer, and assess its potential for the detection of redox changes that occur during chemotherapy.

MATERIALS AND METHODS

Cell lines

Human ovarian cancer A2780 cells were obtained from Sigma-Aldrich, PEO1 and PEO14 cells from Public Health England Culture Collections, and SKOV3 cells were donated by Dr. Anil K. Sood (MD Anderson Cancer Centre, USA). A2780 and SKOV3 cells were selected as well-characterized cell models of human ovarian cancer, with patient-derived PEO1 and PEO14 cells taken from two patients with high grade serous ovarian cancer that were classified as chemotherapy-sensitive. A2780 and SKOV3 cells were cultured in RPMI media supplemented with 10% FBS. PEO1 and PEO14 cells were cultured in RMPI media supplemented with 10% FBS and 2 mM sodium pyruvate. All cell lines were maintained at 37 °C and 5% CO_2 in a humidified atmosphere, with mycoplasma testing performed on a monthly basis. Cells were authenticated by short tandem repeat profiling just prior to submission and kept within 10-15 passages of the original frozen vial.

Animal subjects

Female immunodeficient nu/nu BALB/c mice (8-10 weeks) were used and were obtained from either Charles River Laboratories (UK) or Envigo (UK). Assignment of mice to treatment groups were done randomly. All animal experiments performed at University College London were done in accordance with UK government Animals (Scientific Procedures) Act and according to institutional regulations, with experimental procedures involving animals performed at Stanford University approved by the Stanford University Institutional Animal Care and Use Committee.

Cell drug treatments

Except where specifically noted, cells were seeded 24 h prior to treatment at a density of 5.3×10^4 cells/cm^2 (corresponding to 5×10^5 cells per well on a 6-well plate). For 24 h treatments, seeding densities were: A2780, 5.3×10^4 cells/cm^2; PEO1, 2.6×10^4 cells/cm^2; PEO14, 1.3×10^4 cells/cm^2. Fresh media was provided at least 1 h prior to drug treatments, and for treatment durations 24 h for longer, fresh media including drug was given 1 h prior to any experimental determinations. TBHP was administered 1 h prior to assay at a final concentration of 200 µM. NAC was added 1h prior to TBHP administration (2 h total treatment duration) at a final concentration of 5 mM. Cells were treated with butein (BUT) and diethyl maleate (DEM) 24 h prior to assay, whereas Doxil (DOX) was administered 72 h prior to assay. All remaining drugs were added 1 h prior to assay. Final concentrations were: BUT, 100 µM; rotenone (ROT), 50 µM; auranofin (AUR), 50 µM; antimycin A (AMA), 1.10 µg/mL; DEM, 100 µM; DOX, 200 nM.

Flow cytometric measurement of intracellular reactive oxygen species (ROS) and cell death

Following drug treatment, CellROX Orange or CellROX Green (Invitrogen) was added to each well at a final concentration of 5 µM according to the manufacturer's instructions. For cell death experiments cells were resuspended in 200 µL of HBSS, with Annexin V-Alexa Fluor 488 (5 µL stock/100 µL cell suspension) and Sytox Red (5 nM final concentration) added and samples incubated for 15 min in the dark. Samples were analyzed on a BD LSR Fortessa X-20 flow cytometer. A total of 20,000 single cell events were recorded. Data were gated post-acquisition to include only single cells, and the corresponding fluorescence histograms and median fluorescence intensities (MFI) were extracted using FlowJo software (v. 10.1).

Measurement of intracellular GSH

Cells were seeded at a density of 4×10^4 cells per well in 96-well plates. Following drug treatment, medium was aspirated and the cells were rapidly washed on ice with ice-cold PBS (3×200 µL). GSH measurements were then carried out directly on the plate using the GSH/GSSG-Glo Assay kit (Promega, UK) according to manufacturer's instructions. Estimates of reduced GSH were obtained as the difference between total and oxidised GSH. Data were expressed as the ratio of GSSG:GSH.

Measurement of intracellular glutamate

To examine the relationship between intracellular glutamate and [^{18}F]FSPG retention, cells were incubated for various durations in glutamine/FBS-free media. After all treatments, the medium was aspirated and the cells were washed with 1 mL of warmed Dulbecco's phosphate buffered saline (DPBS). The cells were trypsinized and washed three times by centrifugation ($600 \times g$, 4 °C for 3 min) and resuspension in ice-cold PBS. The final cell pellet was resuspended in 200 µL of ice-cold glutamate assay buffer (Biovision). The cells were then placed on ice and lysed by sonication using a Hielscher UP50H ultrasonic processor for three sets of six 0.5 s pulses. The lysed sample was then centrifuged at $15{,}000 \times g$, 4 °C for 10 min, and the supernatant analyzed using the Biovision Glutamate Colorimetric Assay according to manufacturer's instructions. Protein content was determined using the Pierce BCA Protein Assay Kit (Thermo Fisher) and the glutamate content was expressed as nmol/mg protein.

Metabolomics measurements

For detailed metabolomics protocol please see Supplemental Materials and Methods.

Western blotting

Western blot analysis was accomplished using previous described methodology (34), adapted for use with the iBind Flex system for primary and secondary antibody immunoblotting, according to the manufacturer's instructions. Monoclonal antibodies to rabbit anti-human system x_c^-, GLS, KGA, NRF2, p53, GCL, caspase-3 and cleaved-caspase-3 (1:1000 dilution) were used for western blot analysis of both A2780 cell lysates and tumor lysates. Actin was used as a loading control for all experiments (1:1000 dilution).

***In vivo* tumor model**

Immunocompromised Balb/c nude mice received a subcutaneous injection of 5×10^6 A2780 cells in 100 µL PBS at a location approximately between the scapulae on the dorsal surface. Daily caliper measurements were made on the growing tumors. The volume was estimated by the formula: (length × width × depth × π)/6. When any individual tumor reached 100 mm^3 in volume (day 0), the animal was assigned to one of three groups: untreated, 24 h Doxil treatment, or 6 day Doxil treatment. Untreated animals received no treatment, animals in the 24 h Doxil group received a single intraperitoneal injection of 10 mg/kg Doxil on day 0, and the animals in the 6 d Doxil group received Doxil on days 0, 2 and 5. PET experiments with either [^{18}F]FSPG or [^{18}F]FDG were performed on days 0, 1 and 6 in the untreated, 24 h, and 6 d Doxil treatment groups, respectively. In the [^{18}F]FSPG experiment, each animal was scanned at days 0, 1 and 6, whereas in the [^{18}F]FDG experiment a separate group of animals was scanned on each of the three days. Immediately following [^{18}F]FDG scanning, the tumors were excised, divided into four

approximately equal sized pieces, weighed, rapidly frozen in liquid nitrogen and stored at -80 °C for *ex vivo* analysis.

Ex vivo analysis of tumor tissue samples

Impact-resistant tubes containing Lysing Matrix D (MP Biomedicals) were pre-loaded with 300 µL GSH buffer (Promega), with or without 1 mM *N*-ethyl maleimide (NEM) for determination of GSSG or total GSH, respectively. Separate tubes were pre-loaded with 500 µL of RIPA buffer containing Halt protease and phosphatase inhibitor cocktail (ThermoFisher Scientific) for preparation of samples for Western blot analysis. Into these tubes were placed the tissue samples and the tissue was lysed by rapid shaking for 15 s at 4 °C using a FastPrep-24 homogenizer (MP Biomedicals). The resulting lysates were centrifuged at 15,000 × *g*, 4 °C for 10 min to pellet insoluble debris. The supernatant was analyzed for total glutamate, GSH (oxidized and reduced), and the expression of specific proteins, as described above. Metabolite levels were normalized to sample protein content as described above.

Radiotracer synthesis

The radiotracer [^{18}F]FSPG was prepared using an automated HotBox III module (Scintomics, Fürstenfeldbruck, Germany) (35). The protocol has been adapted from a previously reported method (26). For full details see Supplemental Materials and Methods. [^{18}F]FSPG was obtained with a decay-corrected radiochemical yield of 42 ± 7% (radiochemical purity >99 %, n = 22) after 110-120 min. A final radioactive concentration of up to 221 MBq/mL of formulated tracer was achieved. The specific radioactivity was in the range of 4.2-21.9 GBq/µmol.

Radiotracer cell uptake experiments

Cells were seeded at the appropriate density in 6-well plates (see above). Drug treatments, in triplicate, were carried out as described above, after which 185 kBq of either [^{18}F]FSPG or [^{18}F]FDG was added. After a 60 min uptake period at 37 °C cells were processed according to previously-described methodology (36). Radioactivity in samples was expressed as a percentage of the administered dose per mg protein.

Positron emission tomography experiments

Mice were anaesthetized with isoflurane (2.5% in oxygen) and maintained at 37 °C using an air-heated scanning bed. A cannula was inserted in the tail vein and a 3.7 MBq bolus of either [^{18}F]FSPG or [^{18}F]FDG was administered in approximately 100 µL of PBS. Mice were then allowed to recover from anaesthesia, and forty minutes later a 20 min PET acquisition was performed on a Mediso nanoScan PET/CT system under isoflurane anaesthesia (1.5-2%). Attenuation correction was done using CT data (50 kVp, 480 projections) and static reconstruction was done using the Tera-Tomo 3D reconstruction algorithm, with 4 iterations, 6 subsets, a binning window of 400-600 keV, and a voxel size of 0.4 mm. The resulting reconstructed images were analyzed using VivoQuant software (v. 2.5, Invicro Ltd.). Tumor volumes of interest were compiled from sequential 2D regions of interest drawn on the CT images. The radioactivity concentration in each volume of interest was expressed as a percentage of the injected dose per mL of tissue volume (%ID/mL).

Quantification and statistical analysis

Statistical tests and linear regression analyses were performed using GraphPad Prism software (v. 10.1). Comparisons were considered statistically significant went $p < 0.05$. In all analyses, Bonferroni multiple comparison corrections were applied when appropriate. For normalized flow cytometric data, fold change in median fluorescence intensity was assessed using single sample two-tailed t tests (versus unity). For correlation plots the measure of goodness-of-fit (R^2) was determined, with an F test used to assess whether the line of regression was significantly different from zero. For all other data, standard two-tailed t tests were used.

RESULTS

[^{18}F]FSPG accumulation in tumor cells is altered following manipulation of the intracellular redox environment

In order to evaluate [^{18}F]FSPG accumulation as a surrogate marker of intracellular redox status, A2780 ovarian cancer cells were treated with the oxidant *tert*-butyl hydroperoxide (TBHP), alone or following pre-treatment with the antioxidant *N*-acetylcysteine (NAC), and compared with untreated cells. In response to TBHP alone, cells displayed several hallmark features of oxidative stress: levels of ROS, as measured by the fluorophore CellROX Orange, were elevated 5.6-fold ($p < 0.0001$; **Fig. 1A**), and the ratio of oxidized (GSSG) to reduced GSH was doubled (**Fig. 1B**). In addition, protein expression of the antioxidant transcription factor Nrf2 and the cell cycle regulator p53 were increased upon TBHP treatment (**Fig. 1C**), indicating transcriptional up-regulation of cellular antioxidant defenses, DNA damage and potential cell cycle arrest. TBHP, however, did not induce cell death at this dose, as shown by an absence of cleaved caspase-3 and by flow cytometric measurements using annexin V and Sytox Red (**Fig. 1D**). In contrast, NAC treatment alone did not alter ROS levels (**Fig. 1A**) or the ratio of GSSG to GSH (**Fig. 1B**), suggesting low levels of oxidative stress under baseline cell culture conditions. Following NAC pre-treatment, however, TBHP-mediated oxidative stress was greatly diminished, with the levels of ROS and the ratio of GSSG to GSH similar to untreated cells (**Fig. 1A and B**).

We next examined the accumulation of [^{18}F]FSPG under TBHP/NAC treatment conditions (**Fig. 1E**). Following TBHP-induced oxidative stress, [^{18}F]FSPG cell-associated radioactivity was decreased from 11.0 ± 0.6 % radioactivity/mg protein in untreated cells, to 5.9 ± 1.6 %

radioactivity/mg protein following TBHP treatment ($p < 0.001$; **Fig. 1F**). Decreased [^{18}F]FSPG accumulation was also seen in PEO1, PEO14 and SKOV3 ovarian cancer cells upon TBHP treatment, where it was also associated with increased ROS, demonstrating that [^{18}F]FSPG's sensitivity to redox status was not cell line-specific (**Supplementary Fig. S1**). In A2780 cells, treatment with NAC resulted in a doubling of [^{18}F]FSPG cell-associated radioactivity when administered alone (11.0 ± 0.6 % radioactivity/mg protein in untreated cells and 22.6 ± 3.5 % radioactivity/mg protein following NAC treatment; $p < 0.0001$). When given as a pretreatment, NAC prevented the decrease in [^{18}F]FSPG accumulation seen with TBHP administration (**Fig. 1F**). By comparison, [^{18}F]2-fluoro-2-deoxy-D-glucose ([^{18}F]FDG) uptake, a marker of glucose utilization, was decreased by TBHP, but this effect was not prevented by NAC pre-treatment, nor was there any effect seen following NAC treatment alone (**Fig. 1G**).

Decreased [^{18}F]FSPG accumulation is correlated with the degree of oxidative stress

In order to investigate whether changes in [^{18}F]FSPG accumulation robustly reflected drug-induced oxidative stress, we identified a panel of mechanistically-diverse redox-active compounds and measured their impact on ROS and corresponding changes in [^{18}F]FSPG uptake (**Fig. 2**). The compounds selected were diethyl maleate, an electrophile which causes GSH depletion; antimycin A, an electron transport chain complex III inhibitor; rotenone, an electron transport chain complex I inhibitor; auranofin, a thioredoxin reductase 1 inhibitor; and butein, an inhibitor of signal transducer and activator of transcription 3 (STAT3). In A2780 cells, the magnitude of treatment-induced ROS varied considerably between these compounds, ranging from a 50 % to 330 % increase (**Fig. 2A**). The changes in ROS were paralleled by decreases in [^{18}F]FSPG accumulation, ranging from 15 % to 78 % relative to vehicle-treated control cells **(Fig. 2B**). Importantly, there

was a strong correlation between ROS induction and [^{18}F]FSPG retention ($r = -0.92$, $R^2 = 0.85$, $p = 0.009$; **Fig. 2C**).

Redox-related changes in [^{18}F]FSPG accumulation are associated with alterations in the concentration of intracellular cystine

Having determined that drug-induced oxidative stress paralleled changes in [^{18}F]FSPG accumulation, we next investigated the molecular mechanisms that linked these two outcomes. Levels of xCT protein, the transporter component of heterodimeric system x_c^-, were unchanged by either oxidizing or antioxidant treatments (**Fig. 1C**), ruling out changes in transporter protein expression as an explanation for the observed differences in [^{18}F]FSPG uptake. The extracellular concentrations of the system x_c^- substrates, cystine and glutamate, have previously been shown to affect [^{18}F]FSPG cell uptake (26). Furthermore, both glutamate and cystine are substrates for GSH biosynthesis. We therefore hypothesized that increased GSH biosynthesis under oxidative stress would diminish intracellular pools of cystine and/or glutamate and thereby affect levels of [^{18}F]FSPG retention. A schematic representation of the putative factors influencing [^{18}F]FSPG cell retention is shown in **Fig. 3A**.

The sensitivity of [^{18}F]FSPG retention to levels of intracellular glutamate was tested by incubating cells in glutamine-free media. Removal of glutamine resulted in a rapid depletion of intracellular glutamate, from 107 ± 21 nmol/mg protein to 46 ± 16 nmol/mg protein after 2h glutamine withdrawal ($p < 0.0001$, $n = 3$; **Supplementary Fig. S2**). This glutamate depletion resulted in a concomitant decrease in [^{18}F]FSPG cell-associated radioactivity, from 8.17 ± 0.56 % radioactivity/mg protein to 3.72 ± 0.51 % radioactivity/mg protein ($p < 0.0001$, $n = 3$). Both

[^{18}F]FSPG retention and intracellular glutamate levels were further decreased over the 6 hour time course of glutamine depletion, with [^{18}F]FSPG accumulation strongly correlated to the intracellular concentration of glutamate (R^2 = 0.80, $p < 0.0001$; **Supplementary Fig. S2**). Redox manipulation with TBHP, NAC or the combined treatment, however, had no effect on intracellular or extracellular glutamate in A2780 cells (**Fig. 3B and C**; $p > 0.05$, n = 3-4), nor were there changes in expression of glutaminase enzymes which serve as a major source of cellular glutamate through glutaminolysis (**Fig. 1C**). In contrast, intracellular cystine concentrations mirrored the pattern of [^{18}F]FSPG accumulation (**Fig. 3D**), with lowered cystine measured in lysates from TBHP-treated cells, increased cystine present following NAC treatment, and intermediate levels seen after the combined treatment. NAC treatment also dramatically decreased extracellular cystine levels (**Fig. 3E**), whereas TBHP had no such effect. In addition, [^{18}F]FSPG cell retention was markedly dependent on the concentration of extracellular cystine (**Supplementary Fig. S2**).

Oxidative stress decreases intracellular cystine via stimulation of GSH biosynthesis.

We next used isotopic tracing to identify the mechanism underlying the changes in cystine that follow oxidative stress. We incubated A2780 cells in cystine-free media supplemented with [U-$^{13}C_6$, U-$^{15}N_2$]cystine to isotopically follow the fate of cystine through key metabolites in the GSH biosynthetic pathway, shown in **Fig. 4A**. TBHP treatment resulted in a large and progressive decrease in intracellular [U-$^{13}C_6$, U-$^{15}N_2$]cystine (**Fig. 4B**), confirming our previous steady-state measurements. Heavy isotope-labeled cysteine was also reduced upon TBHP treatment (**Fig. 4C**), however, a small increase in isotopic enrichment was seen for γ-glutamylcysteine (**Fig. 4D**) and reduced GSH (**Fig. 4E**) under these oxidizing conditions. Looking to the furthest point downstream (**Fig. 4F**), TBHP treatment resulted in increased isotopic enrichment of both single (M+4) and dual

(M+8) labeled GSSG, indicating that increased flux into GSH biosynthesis is at least partly responsible for the decrease in intracellular cystine. Incorporation of two heavy-labeled cystines into GSSG occurred at a slower rate than single label incorporation given the large preexisting pool of unlabeled GSH, with elevated flux of cystine into M+8 GSSG following TBHP treatment evident by 60 min (**Supplementary Fig. S3**). NAC-induced cystine changes were also investigated using a steady-state approach with unlabeled cystine. Here, we found that the decrease in extracellular cystine upon NAC treatment (**Fig. 2D**) was the result of a disulfide exchange reaction in which cystine is largely replaced by a NAC-cysteine disulfide species (**Supplementary Fig. S4**). This disulfide exchange reaction also occurred intracellularly, as evidenced by the appearance of the NAC-cysteine conjugate.

[^{18}F]FSPG PET detects changes in tumor redox status prior to tumor shrinkage or decreased [^{18}F]FDG uptake.

We next examined the effect of the commonly-used chemotherapeutic doxorubicin on *in vivo* [^{18}F]FSPG tumor retention as a surrogate marker of therapy response. Using the liposomal form of the drug (Doxil), we first confirmed the effect of doxorubicin on [^{18}F]FSPG accumulation and intracellular markers of oxidative stress in A2780 ovarian cancer cells grown in culture. As shown in **Supplementary Fig. S5**, 72h Doxil treatment resulted in a large decrease in [^{18}F]FSPG cell-associated radioactivity from 10.8 ± 1.6 to 2.5 ± 0.1 % radioactivity/mg protein ($p < 0.001$) which was associated with increased ROS, a decrease in total GSH, and an increase in the ratio of GSSG to GSH.

In A2780 ovarian tumor-bearing mice, [^{18}F]FSPG PET was characterized by high uptake in the tumor and pancreas, tissues with elevated system x_c^--expression. The remaining activity was cleared via the urinary tract to produce excellent tumor-to-background contrast (**Supplementary Fig. S6**). A2780 tumor-bearing mice were subsequently treated with Doxil over a six day treatment time course (**Fig. 5A**), with tumor response to therapy imaged by [^{18}F]FSPG PET. Tumor growth rate was unaffected by a single bolus of Doxil (**Fig. 5B**), however a second round of treatment resulted in a reduction in tumor volume between days 3 and 6, yielding tumors on day 6 that were similar in volume to their original size prior to therapy. In tumors, total GSH dropped from 19.1 ± 2.3 nmol/mg protein to 12.6 ± 3.0 nmol/mg protein ($p < 0.05$) just 24 h post-Doxil treatment (**Fig. 5C**), indicating changes in tumor redox status that precede, by two days, a reduction in tumor volume indicative of chemotherapy response. Further changes in tumor redox status were seen in the ratio of GSSG to GSH, which increased over the course of treatment from 0.010 ± 0.005 to 0.27 ± 0.18 after 6 days treatment ($p < 0.01$; **Fig. 5D**). Doxil treatment increased levels of p53, and to a lesser extent cleaved caspase-3, providing further evidence of a positive response to therapy (**Supplementary Fig. S6**). Surprisingly, no increase in levels of the antioxidant transcription factor Nrf2 or the GSH biosynthetic enzyme glutamate-cysteine ligase (GCL) were observed. There were also no changes in tumor xCT protein levels with Doxil treatment (**Supplementary Fig. S6**).

In tumors, [^{18}F]FSPG retention decreased by 42% just 24 h after Doxil treatment, from 4.35 ± 0.87 % ID/mL in untreated animals (**Movie S1**), to 2.25 ± 0.91 % ID/mL ($p < 0.01$; **Fig. 5E, F and Movie S2**). This decrease in tumor-associated [^{18}F]FSPG coincided with Doxil-induced depletion of GSH (**Fig. 5C**), but occurred prior to any observable tumor shrinkage, (**Fig. 5B**). Decreased [^{18}F]FSPG tumor retention was still evident 6 days after treatment (2.28 ± 1.23 %ID/g, $p < 0.01$

relative to untreated mice; **Movie S3**). Representative sagittal and axial images are shown in **Supplementary Fig. S6**. By comparison, [^{18}F]FDG uptake was unchanged after 24 h of treatment, when tumor redox changes became apparent, but was significantly decreased at the 6 day time point, from 4.85 ± 1.29 % ID/mL on D0 to 2.28 ± 1.23 % ID/mL on D6, when tumor shrinkage was evident ($p < 0.05$; **Supplementary Fig. S6**).

DISCUSSION

Despite the clinical importance of tumor antioxidant responses, development of non-invasive tools for the assessment of this highly-regulated system remains a major unmet clinical need. Here, we have shown that the PET radiotracer [^{18}F]FSPG, already used in pilot clinical trials, can be used to monitor spatiotemporal changes in redox status. A key finding of this study is that [^{18}F]FSPG tumor retention provides an index of redox status through its sensitivity to levels of intracellular cystine. System x_c^--derived cystine plays a central role in redox biochemistry. Indeed, pharmacological inhibition of system x_c^- results in greatly reduced cellular GSH (37) and system x_c^- knock out mice show decreased levels of GSH in the blood (38). Intracellularly, system x_c^--derived cystine is rapidly reduced to cysteine, which itself plays a crucial role in antioxidant processes. In addition to its role in GSH biosynthesis, cysteine can act as an antioxidant, protecting the cell during conditions of GSH depletion (39). Transmembrane cycling of the cystine-cysteine redox pair is also important in maintenance of both intra- and extracellular redox homeostasis (40). Cystine levels therefore represent a point of convergence between multiple arms of the cell's antioxidant system, making the responsiveness of [^{18}F]FSPG uptake to this amino acid a valuable surrogate marker of oxidative stress.

The changes that we observe in [^{18}F]FSPG retention with oxidative stress can be understood by considering the mechanism of system x_c^- transport. The cystine/glutamate exchange activity of system x_c^- is mediated by the membrane concentration gradients of the exchanged species, glutamate (high intracellular, low extracellular) and cystine (low intracellular, high extracellular) (27). Consequently, both amino acids are exchanged along their concentration gradients, with

glutamate leaving and cystine entering the cell. [^{18}F]FSPG acts as a third exchange partner in this exchange system, and as expected, its cell retention was influenced by levels of cystine or glutamate. Additionally, both cystine and glutamate can act competitively (41), preventing interaction of [^{18}F]FSPG with system x_c^- (26). Thus, there are two potential mechanisms by which changes in levels of cystine or glutamate could affect [^{18}F]FSPG retention: through changes in the amino acid gradients across the plasma membrane, or through altered levels of competition at the site of the transporter. A schematic depicting these processes is shown in **Fig. 3A.** Kinetic analysis of dynamic imaging data may help further elucidate the mechanism of [^{18}F]FSPG trapping and retention, taking into account both cellular transport and blood flow. Our findings confirm the sensitivity of [^{18}F]FSPG retention to changes in levels of either amino acid (**Fig. 3** and **Supplementary Fig. S2**). However, during oxidative stress glutamate levels remain unchanged, implicating the observed depletion of intracellular cystine as the factor mediating changes in [^{18}F]FSPG uptake.

Using a metabolomics approach, we explored the connection between oxidative stress and changes in cystine metabolism. We found that the decrease in intracellular cystine following TBHP treatment was the result of an increase in flux of cystine through the GSH biosynthetic pathway. Using heavy isotope-labeled cystine, TBHP produced a selective isotopic enrichment of GSSG, indicating increased GSH biosynthesis and subsequent oxidation. This finding provides a direct mechanistic connection between oxidative stress, intracellular cystine levels and [^{18}F]FSPG uptake. Isotopic enrichment of reduced GSH was only marginally increased in stressed over untreated cells, probably reflecting both the far larger GSH pool compared to GSSG (100×) and the relatively short enrichment time of 60 min. Whereas oxidative stress changed only intracellular

cystine levels, the antioxidant NAC altered both intracellular and extracellular concentrations of cystine. The extracellular changes were accounted for by a disulfide exchange reaction between NAC and cystine, which converted virtually all extracellular cystine to free cysteine and a NAC-cysteine mixed disulfide species. NAC also resulted in an increase in intracellular cystine, potentially by providing cysteine through deacetylation of NAC (42).

Unlike other redox imaging methods currently under development, which monitor ROS levels via oxidation/reduction of a probe compound, [^{18}F]FSPG PET does not provide an index ROS production *per se*. Rather, it provides a measure of cellular antioxidant response (i.e. increased GSH biosynthesis). An advantage of this approach is that adaptive changes such as increased GSH biosynthesis represent processes down-stream of ROS and are therefore more proximal to desired outcomes such as cell death. Indeed, rather than killing cells directly, ROS induce intervening redox biochemical changes, including GSH depletion and alteration of thiol/disulfide balance, which in turn trigger apoptosis (43). While we have provided evidence that glutamate levels are unaltered during oxidative stress, it is possible that non-redox related changes in glutamate, such as those associated with glutamate utilization in anaplerosis and energy metabolism, could confound interpretation of [^{18}F]FSPG PET data. Nevertheless, our results suggest that during drug-induced oxidative stress changes in [^{18}F]FSPG retention are selectively mediated by the alteration of intracellular cystine. Furthermore, [^{18}F]FSPG PET currently represents the only non-invasive imaging method to have reached a stage of development appropriate for further translation to human redox imaging studies.

Several therapeutic strategies, including chemotherapy, radiotherapy and targeted therapies act in-part to disrupt tumor redox homeostasis (44-46). As a consequence, the emergence of resistance to these therapies is often accompanied by enhanced antioxidant production (13). Specifically, doxorubicin's therapeutic mechanism of action involves both the direct and indirect induction of oxidative stress oxidative stress via redox cycling, production of superoxide and hydrogen peroxide, and DNA damage (47). Tumor-associated [^{18}F]FSPG was sensitive to doxil-induced changes in tumor redox status which occurred soon after the initiation of treatment but prior to measurable changes in tumor volume (**Fig. 5**). In particular, Doxil caused a depletion of tumor GSH potentially as either the direct result of Doxil-induced oxidative stress or via formation and efflux of Doxil-GSH conjugate by the multidrug-resistance-associated proteins (MRPs) (48). GSH depletion by either mechanism could presumably affect intracellular cystine levels by influencing *de novo* GSH synthesis. Therefore, [^{18}F]FSPG could facilitate a precision medicine approach in which drug response could be predicted in individual patients based on redox response measurements. Moreover, given that steady-state levels of GSH are known to correlate well with drug resistance, a dynamic marker of GSH biosynthetic flux may provide further insights into drug resistance mechanisms *in vivo*.

In conclusion, this study demonstrates in preclinical models of cancer, that a PET radiotracer used in clinical investigations is sensitive to tumor redox status. Oxidative stress-induced changes in [^{18}F]FSPG retention were mediated by alterations of intracellular cystine, the dimeric form of cysteine, that is central to cellular responses to oxidative challenge. [^{18}F]FSPG therefore represents a potentially valuable PET imaging agent for investigation of redox status in human disease. In

cancer imaging, [^{18}F]FSPG may show particular value given the importance of redox mechanisms in tumorigenesis, treatment response and the development of drug resistance.

ACKNOWLEDGMENTS

The authors would like to thank Andrew Stephens and Stephen Patrick for helpful theoretical discussions, Bernadette Schneider for technical support regarding [^{18}F]FSPG radiochemistry, William Day for help with flow cytometric experiments, and May Zaw-Thin for assistance during PET scanning. The authors also acknowledge the SCi3 Small Animal Imaging Service Center, which was used to create data presented in this study, specifically, Tim Doyle and Israt Alam for their valuable assistance. This study was funded through a Wellcome Trust and Royal Society Sir Henry Dale Fellowship (107610/Z/15/Z) and the Cancer Research UK-UCL Centre (C416/A18088) to Timothy Witney, the CRUK & EPSRC Comprehensive Cancer Imaging Centre at KCL & UCL (C1519/A16463) to Erik Årstad, and financial support from Life Molecular Imaging GmbH (formally Piramal Imaging) to Timothy Witney and Sanjiv Sam Gambhir. UCL radiochemistry is funded in-part by the Department of Health's NIHR Biomedical Research Centres funding scheme.

REFERENCES

1. Sabharwal SS, Schumacker PT. Mitochondrial ROS in cancer: initiators, amplifiers or an Achilles' heel? Nat Rev Cancer. 2014;14:709-21.
2. Gao X, Schottker B. Reduction-oxidation pathways involved in cancer development: a systematic review of literature reviews. Oncotarget. 2017;8:51888-906.
3. Reuter S, Gupta SC, Chaturvedi MM, Aggarwal BB. Oxidative stress, inflammation, and cancer: how are they linked? Free Radic Biol Med. 2010;49:1603-16.
4. Kardes S, Karagulle M, Durak I, Avci A, Karagulle MZ. Association of oxidative stress with clinical characteristics in patients with rheumatoid arthritis. Eur J Clin Invest. 2018;48.
5. Sugamura K, Keaney JF, Jr. Reactive oxygen species in cardiovascular disease. Free Radic Biol Med. 2011;51:978-92.
6. Barnham KJ, Masters CL, Bush AI. Neurodegenerative diseases and oxidative stress. Nat Rev Drug Discov. 2004;3:205-14.
7. Vander Heiden MG, DeBerardinis RJ. Understanding the Intersections between Metabolism and Cancer Biology. Cell. 2017;168:657-69.
8. Szatrowski TP, Nathan CF. Production of large amounts of hydrogen peroxide by human tumor cells. Cancer Res. 1991;51:794-8.
9. Harris IS, Treloar AE, Inoue S, Sasaki M, Gorrini C, Lee KC, et al. Glutathione and thioredoxin antioxidant pathways synergize to drive cancer initiation and progression. Cancer Cell. 2015;27:211-22.
10. Faber M, Coudray C, Hida H, Mousseau M, Favier A. Lipid peroxidation products, and vitamin and trace element status in patients with cancer before and after chemotherapy, including adriamycin. A preliminary study. Biol Trace Elem Res. 1995;47:117-23.
11. Sangeetha P, Das UN, Koratkar R, Suryaprabha P. Increase in free radical generation and lipid peroxidation following chemotherapy in patients with cancer. Free Radic Biol Med. 1990;8:15-9.
12. Weijl NI, Hopman GD, Wipkink-Bakker A, Lentjes EG, Berger HM, Cleton FJ, et al. Cisplatin combination chemotherapy induces a fall in plasma antioxidants of cancer patients. Ann Oncol. 1998;9:1331-7.
13. Liu Y, Li Q, Zhou L, Xie N, Nice EC, Zhang H, et al. Cancer drug resistance: redox resetting renders a way. Oncotarget. 2016;7:42740-61.
14. Chu W, Chepetan A, Zhou D, Shoghi KI, Xu J, Dugan LL, et al. Development of a PET radiotracer for non-invasive imaging of the reactive oxygen species, superoxide, in vivo. Org Biomol Chem. 2014;12:4421-31.
15. Hou C, Hsieh CJ, Li S, Lee H, Graham TJ, Xu K, et al. Development of a Positron Emission Tomography Radiotracer for Imaging Elevated Levels of Superoxide in Neuroinflammation. ACS Chem Neurosci. 2018;9:578-86.
16. Wilson AA, Sadovski O, Nobrega JN, Raymond RJ, Bambico FR, Nashed MG, et al. Evaluation of a novel radiotracer for positron emission tomography imaging of reactive oxygen species in the central nervous system. Nucl Med Biol. 2017;53:14-20.
17. Webster JM, Morton CA, Johnson BF, Yang H, Rishel MJ, Lee BD, et al. Functional imaging of oxidative stress with a novel PET imaging agent, 18F-5-fluoro-L-aminosuberic acid. J Nucl Med. 2014;55:657-64.

18. Yang H, Jenni S, Colovic M, Merkens H, Poleschuk C, Rodrigo I, et al. (18)F-5-Fluoroaminosuberic Acid as a Potential Tracer to Gauge Oxidative Stress in Breast Cancer Models. J Nucl Med. 2017;58:367-73.
19. Sowers MA, McCombs JR, Wang Y, Paletta JT, Morton SW, Dreaden EC, et al. Redox-responsive branched-bottlebrush polymers for in vivo MRI and fluorescence imaging. Nat Commun. 2014;5:5460.
20. Bohndiek SE, Kettunen MI, Hu DE, Kennedy BW, Boren J, Gallagher FA, et al. Hyperpolarized [1-13C]-ascorbic and dehydroascorbic acid: vitamin C as a probe for imaging redox status in vivo. J Am Chem Soc. 2011;133:11795-801.
21. Eto H, Hyodo F, Kosem N, Kobayashi R, Yasukawa K, Nakao M, et al. Redox imaging of skeletal muscle using in vivo DNP-MRI and its application to an animal model of local inflammation. Free Radic Biol Med. 2015;89:1097-104.
22. Baek S, Choi CM, Ahn SH, Lee JW, Gong G, Ryu JS, et al. Exploratory clinical trial of (4S)-4-(3-[18F]fluoropropyl)-L-glutamate for imaging xC- transporter using positron emission tomography in patients with non-small cell lung or breast cancer. Clin Cancer Res. 2012;18:5427-37.
23. Baek S, Mueller A, Lim YS, Lee HC, Lee YJ, Gong G, et al. (4S)-4-(3-18F-fluoropropyl)-L-glutamate for imaging of xC transporter activity in hepatocellular carcinoma using PET: preclinical and exploratory clinical studies. J Nucl Med. 2013;54:117-23.
24. Mittra ES, Koglin N, Mosci C, Kumar M, Hoehne A, Keu KV, et al. Pilot Preclinical and Clinical Evaluation of (4S)-4-(3-[18F]Fluoropropyl)-L-Glutamate (18F-FSPG) for PET/CT Imaging of Intracranial Malignancies. PLoS One. 2016;11:e0148628.
25. Kavanaugh G, Williams J, Morris AS, Nickels ML, Walker R, Koglin N, et al. Utility of [(18)F]FSPG PET to Image Hepatocellular Carcinoma: First Clinical Evaluation in a US Population. Mol Imaging Biol. 2016;18:924-34.
26. Koglin N, Mueller A, Berndt M, Schmitt-Willich H, Toschi L, Stephens AW, et al. Specific PET imaging of xC- transporter activity using a (1)(8)F-labeled glutamate derivative reveals a dominant pathway in tumor metabolism. Clin Cancer Res. 2011;17:6000-11.
27. Bannai S, Ishii T. A novel function of glutamine in cell culture: utilization of glutamine for the uptake of cystine in human fibroblasts. J Cell Physiol. 1988;137:360-6.
28. Pader I, Sengupta R, Cebula M, Xu J, Lundberg JO, Holmgren A, et al. Thioredoxin-related protein of 14 kDa is an efficient L-cystine reductase and S-denitrosylase. Proc Natl Acad Sci U S A. 2014;111:6964-9.
29. Griffith OW. Biologic and pharmacologic regulation of mammalian glutathione synthesis. Free Radic Biol Med. 1999;27:922-35.
30. Hansen RE, Roth D, Winther JR. Quantifying the global cellular thiol-disulfide status. Proc Natl Acad Sci U S A. 2009;106:422-7.
31. Bannai S. Induction of cystine and glutamate transport activity in human fibroblasts by diethyl maleate and other electrophilic agents. J Biol Chem. 1984;259:2435-40.
32. Muir A, Danai LV, Gui DY, Waingarten CY, Lewis CA, Vander Heiden MG. Environmental cystine drives glutamine anaplerosis and sensitizes cancer cells to glutaminase inhibition. Elife. 2017;6.
33. Sayin VI, LeBoeuf SE, Singh SX, Davidson SM, Biancur D, Guzelhan BS, et al. Activation of the NRF2 antioxidant program generates an imbalance in central carbon metabolism in cancer. Elife. 2017;6.

34. Witney TH, Kettunen MI, Day SE, Hu DE, Neves AA, Gallagher FA, et al. A comparison between radiolabeled fluorodeoxyglucose uptake and hyperpolarized (13)C-labeled pyruvate utilization as methods for detecting tumor response to treatment. Neoplasia. 2009;11:574-82, 1 p following 82.
35. Glaser M, Gendron T, McCormick PN, Berndt M, Koglin N, Sander K, et al. Automated Radiosynthesis and Biological Evaluation of [18F]FSPG. J Label Comp Radiopharm. 2017;60:S171.
36. Witney TH, James ML, Shen B, Chang E, Pohling C, Arksey N, et al. PET imaging of tumor glycolysis downstream of hexokinase through noninvasive measurement of pyruvate kinase M2. Sci Transl Med. 2015;7:310ra169.
37. Doxsee DW, Gout PW, Kurita T, Lo M, Buckley AR, Wang Y, et al. Sulfasalazine-induced cystine starvation: potential use for prostate cancer therapy. Prostate. 2007;67:162-71.
38. Sato H, Shiiya A, Kimata M, Maebara K, Tamba M, Sakakura Y, et al. Redox imbalance in cystine/glutamate transporter-deficient mice. J Biol Chem. 2005;280:37423-9.
39. Mandal PK, Seiler A, Perisic T, Kolle P, Banjac Canak A, Forster H, et al. System x(c)- and thioredoxin reductase 1 cooperatively rescue glutathione deficiency. J Biol Chem. 2010;285:22244-53.
40. Jonas CR, Ziegler TR, Gu LH, Jones DP. Extracellular thiol/disulfide redox state affects proliferation rate in a human colon carcinoma (Caco2) cell line. Free Radic Biol Med. 2002;33:1499-506.
41. Bannai S, Kitamura E. Transport interaction of L-cystine and L-glutamate in human diploid fibroblasts in culture. J Biol Chem. 1980;255:2372-6.
42. Rushworth GF, Megson IL. Existing and potential therapeutic uses for N-acetylcysteine: the need for conversion to intracellular glutathione for antioxidant benefits. Pharmacol Ther. 2014;141:150-9.
43. Franco R, Cidlowski JA. Apoptosis and glutathione: beyond an antioxidant. Cell Death Differ. 2009;16:1303-14.
44. Azzam EI, Jay-Gerin JP, Pain D. Ionizing radiation-induced metabolic oxidative stress and prolonged cell injury. Cancer Lett. 2012;327:48-60.
45. Conklin KA. Chemotherapy-associated oxidative stress: impact on chemotherapeutic effectiveness. Integr Cancer Ther. 2004;3:294-300.
46. Teppo HR, Soini Y, Karihtala P. Reactive Oxygen Species-Mediated Mechanisms of Action of Targeted Cancer Therapy. Oxid Med Cell Longev. 2017;2017:1485283.
47. Shevchuk OO, Posokhova EA, Sakhno LA, Nikolaev VG. Theoretical ground for adsorptive therapy of anthracyclines cardiotoxicity. Exp Oncol. 2012;34:314-22.
48. Zaman GJ, Lankelma J, van Tellingen O, Beijnen J, Dekker H, Paulusma C, et al. Role of glutathione in the export of compounds from cells by the multidrug-resistance-associated protein. Proc Natl Acad Sci U S A. 1995;92:7690-4.

FIGURE LEGENDS

Figure 1. [^{18}F]FSPG accumulation is altered following manipulation of the intracellular redox environment. (A) Flow cytometric measurement of total reactive oxygen species (ROS) levels using CellROX Orange, following treatment with TBHP (200 μM, 1 h), NAC (5 mM, 2 h), or the combined treatment (BOTH). **(i)** Representative CellROX Orange fluorescence histograms. **(ii)** Fold-change in median CellROX Orange fluorescence intensity relative to untreated cells (UT). Scatter plot points represent data from independent experiments, each performed as a single measurement. **(B)** Intracellular ratio of oxidized (GSSG) to reduced GSH following treatment with TBHP, NAC or BOTH. Scatter plot points represent independent experiments performed in duplicate or triplicate. **(C)** Western blot showing changes in protein expression following treatment with TBHP, NAC or BOTH. KGA and GAC, splice variants of K-type mitochondrial glutaminase; Nrf2, Nuclear factor (erythroid-derived 2)-like 2; Casp-3, inactive form of caspase 3; ΔCasp-3, active (cleaved) form of Casp-3. **(D)** Flow cytometric data in (i) UT and (ii) TBHP-treated cells showing levels of cell death as detected with Annexin V-alexafluor 488 (λ Ex/Em = 488/535) and Sytox Red staining (λ Ex/Em = 633/658). Q1 = viable; Q2 = early apoptotic; Q3 = late apoptotic/necrotic. **(E)** Molecular structure of [^{18}F]FSPG. **(F and G)** Intracellular retention of [^{18}F]FSPG **(F)** and [^{18}F]FDG **(G)** following treatment with TBHP, NAC or BOTH. Scatter plot points represent independent experiments performed in triplicate. Data are presented as mean ± SD. ††† $p < 0.001$, Bonferroni multiple comparison-corrected single sample t test (versus unity); **** $p < 0.0001$, ** $p < 0.01$, *** $p < 0.001$, Bonferroni multiple comparison-corrected t test. TBHP, tert-butyl hydroperoxide; NAC, N-acetylcysteine.

Figure 2. Decreased [^{18}F]FSPG accumulation is correlated with the degree of oxidative stress. (A) Intracellular fluorescence of the reactive oxygen species (ROS)-sensitive fluorophore CellROX Green following treatment with vehicle (dimethyl sulfoxide, DMSO) or the ROS-inducing compounds diethyl maleate (DEM, 100 μM, 24 h), antimycin A (AMA, 110 μg/mL, 1 h), rotenone (ROT, 50 μM, 1 h), auranofin (AUR, 50 μM, 1 h), butein (100 μM, 24 h). Scatter plot points represent data from independent experiments, each performed as a single measurement. **(B)**

Intracellular retention of [^{18}F]FSPG following the above treatments. Scatter plot points represent independent experiments, each performed as a single measurement. **(C)** Correlation between CellROX Green fluorescence and intracellular [^{18}F]FSPG accumulation. Broken lines represent the 95% confidence interval of the best fit line. Data are presented as mean ± SD. * $p < 0.05$, ** $p < 0.01$, *** $p < 0.001$, single sample t test (versus unity). For scatter plots, an F test was used to determine whether the line of best fit was significantly different from zero.

Figure 3. Changes in [^{18}F]FSPG accumulation are associated with alteration of intracellular cystine concentration. (A) Model of mechanisms influencing [^{18}F]FSPG retention. Intracellular [^{18}F]FSPG accumulation (black arrows indicate influx and efflux) is mediated by system x_c^--mediated exchange with glutamate and cystine. The concentration gradients (wedges) and physiologically-relevant exchange directions (arrows) of glutamate (green) and cystine (red) are indicated. In addition to the influence of concentration gradients, both cystine and glutamate can compete with [^{18}F]FSPG for binding to xCT, thereby inhibiting [^{18}F]FSPG transport. Sites of competition are schematically illustrated as green and red asterisks. o and i represent extracellular and intracellular compartments, respectively. **(B and C)** Intracellular **(B)** and extracellular **(C)** levels of glutamate (Glu) following treatment with TBHP, NAC, or the combined treatment (BOTH). Data are presented as mean ± SD. Scatter plot points represent independent experiments performed in duplicate or triplicate. **(D and E)** Intracellular **(D)** and extracellular **(E)** levels of cystine following treatment with TBHP, NAC, or BOTH. Data are presented as mean ± SD. Scatter plot points represent replicate wells.

Figure 4. Oxidative stress decreases intracellular cystine via stimulation of GSH biosynthesis. (A) Cells were fed with [U-$^{13}C_6$, U-$^{15}N_2$]cystine (200 μM) and the fate of the isotopic label within the GSH biosynthetic pathway was followed in cell lysates using LC-MS. Red dots indicate the position of carbon-13/nitogen-15 label. **(B-F)** Intracellular levels of labelled metabolites in lysates from untreated cells and cells treated with TBHP (200 μM, 1 h). **(B)** cystine [$(Cys)_2$, M+8 molecular species]; **(C)** cysteine (Cys, M+4); **(D)** γ-glutamylcysteine (γ-GC, M+4); **(E)** reduced GSH (M+4); and **(F)** oxidized GSH (GSSG, M+4). Data are presented as mean ± SD

of three replicate wells. Trx, thioredoxin; TrxR1, thioredoxin reductase 1; GCL, glutamate-cysteine ligase; GS, glutathione synthetase; Gly, glycine. o and i represent extracellular and intracellular compartments, respectively.

Figure 5. Treatment with the chemotherapeutic Doxil causes changes in tumor redox status that precede tumor shrinkage. (A) Doxil treatment regime. Mice received s.c. inoculation of A2780 ovarian cancer cells. Day 0 (D0) was defined for each mouse as the day at which its tumor reached 100 mm^3 (10-12 d growth). Mice were then assigned to either the untreated, 24 h (D1) or 6 day (D6) treatment groups. The untreated group was imaged on D0. The 24 h treatment group received Doxil treatment (10 mg/kg, i.p.) on D0 and was imaged on D1, and to the 6 day treatment group received Doxil treatment on D0, D2 and D5 and was imaged on D6. **(B)** Tumor growth curves in untreated mice (D0) and mice treated with Doxil for 24 h (D1) or 6 days (D6). Data represent mean ± SD (n = 4-5 mice). **(C and D)** Total GSH **(C)** levels and the ratio of GSSG to GSH **(D)** in tumors excised after imaging. Scatter plot points represent measurements from individual animals performed in duplicate or triplicate. **(E)** Representative [^{18}F]FSPG PET volume rendered technique PET/CT images from mice receiving no Doxil (D0), 24 h (D1) or 6 days of Doxil treatment (D6). Tumors are indicated by white arrows. **(F)** Quantified [^{18}F]FSPG tumor retention in mice treated as above. * $p < 0.05$, ** $p < 0.01$, *** $p < 0.001$, $p < 0.0001$, Bonferroni multiple comparison-corrected t test versus D0 group.

FIGURE 1

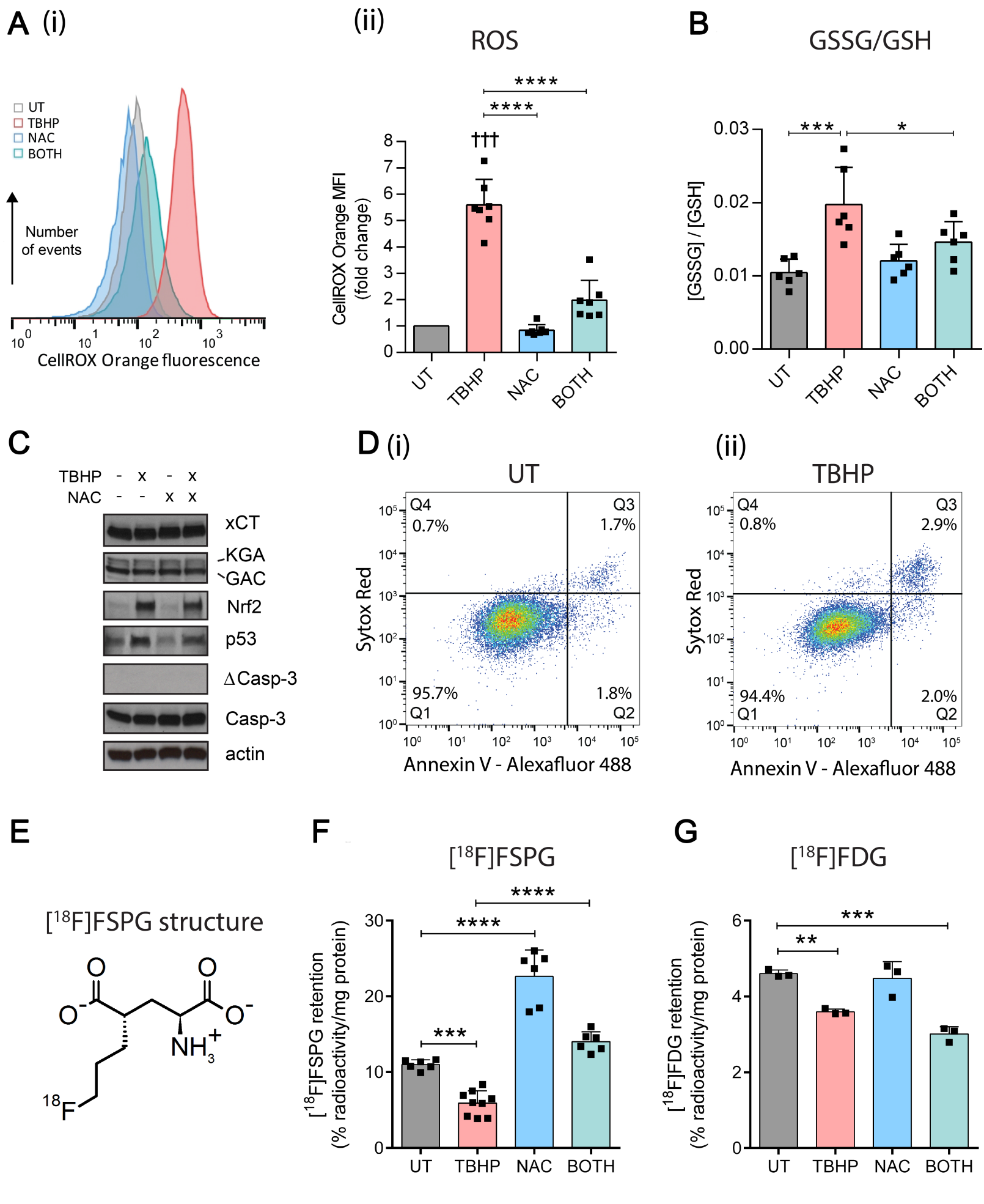
A (i)
UT
TBHP
NAC
BOTH
Number of events
CellROX Orange fluorescence
(ii)
ROS
CellROX Orange MFI (fold change)
****
****
†††
UT
TBHP
NAC
BOTH
B
GSSG/GSH
[GSSG] / [GSH]
***
*
C
TBHP - x - x
NAC - - x x
xCT
KGA
GAC
Nrf2
p53
ΔCasp-3
Casp-3
actin
D (i)
UT
Sytox Red
Q4 0.7%
Q3 1.7%
95.7% Q1
1.8% Q2
Annexin V - Alexafluor 488
(ii)
TBHP
Q4 0.8%
Q3 2.9%
94.4% Q1
2.0% Q2
E
[18F]FSPG structure
F
[18F]FSPG
[18F]FSPG retention (% radioactivity/mg protein)
G
[18F]FDG
[18F]FDG retention (% radioactivity/mg protein)

FIGURE 2

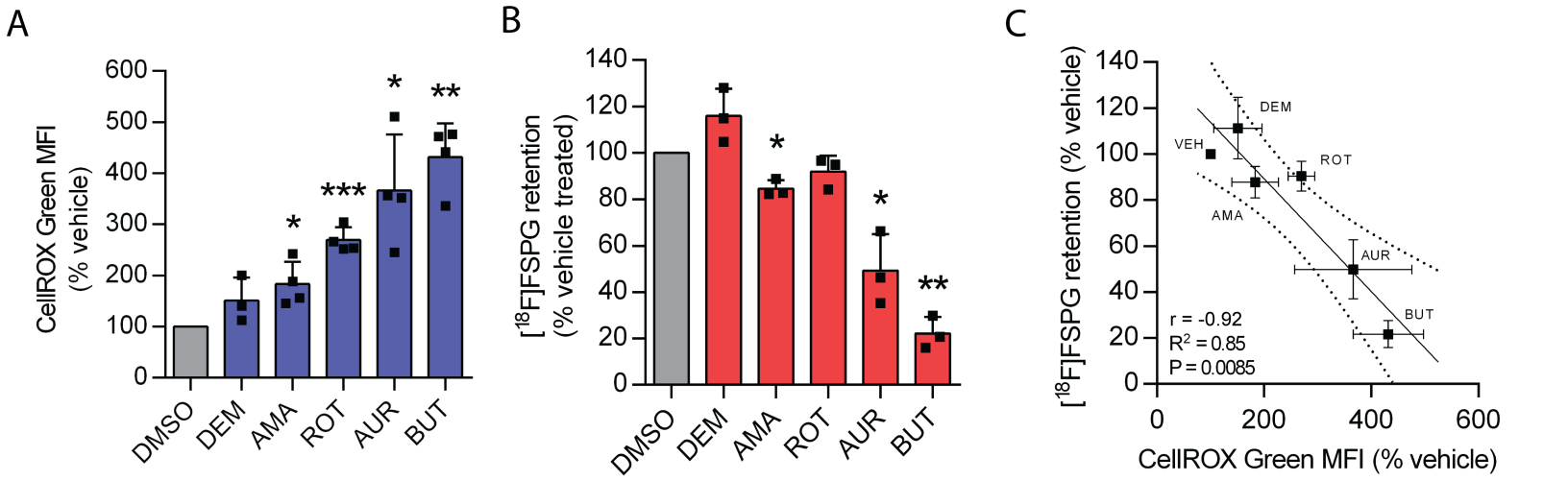
A
CellROX Green MFI
(% vehicle)
600
500
400
300
200
100
0
*
***
*
**
DMSO
DEM
AMA
ROT
AUR
BUT
B
[18F]FSPG retention
(% vehicle treated)
140
120
100
80
60
40
20
0
*
*
**
DMSO
DEM
AMA
ROT
AUR
BUT
C
[18F]FSPG retention (% vehicle)
140
120
100
80
60
40
20
0
VEH
DEM
ROT
AMA
AUR
BUT
r = -0.92
R2 = 0.85
P = 0.0085
0
200
400
600
CellROX Green MFI (% vehicle)

FIGURE 3

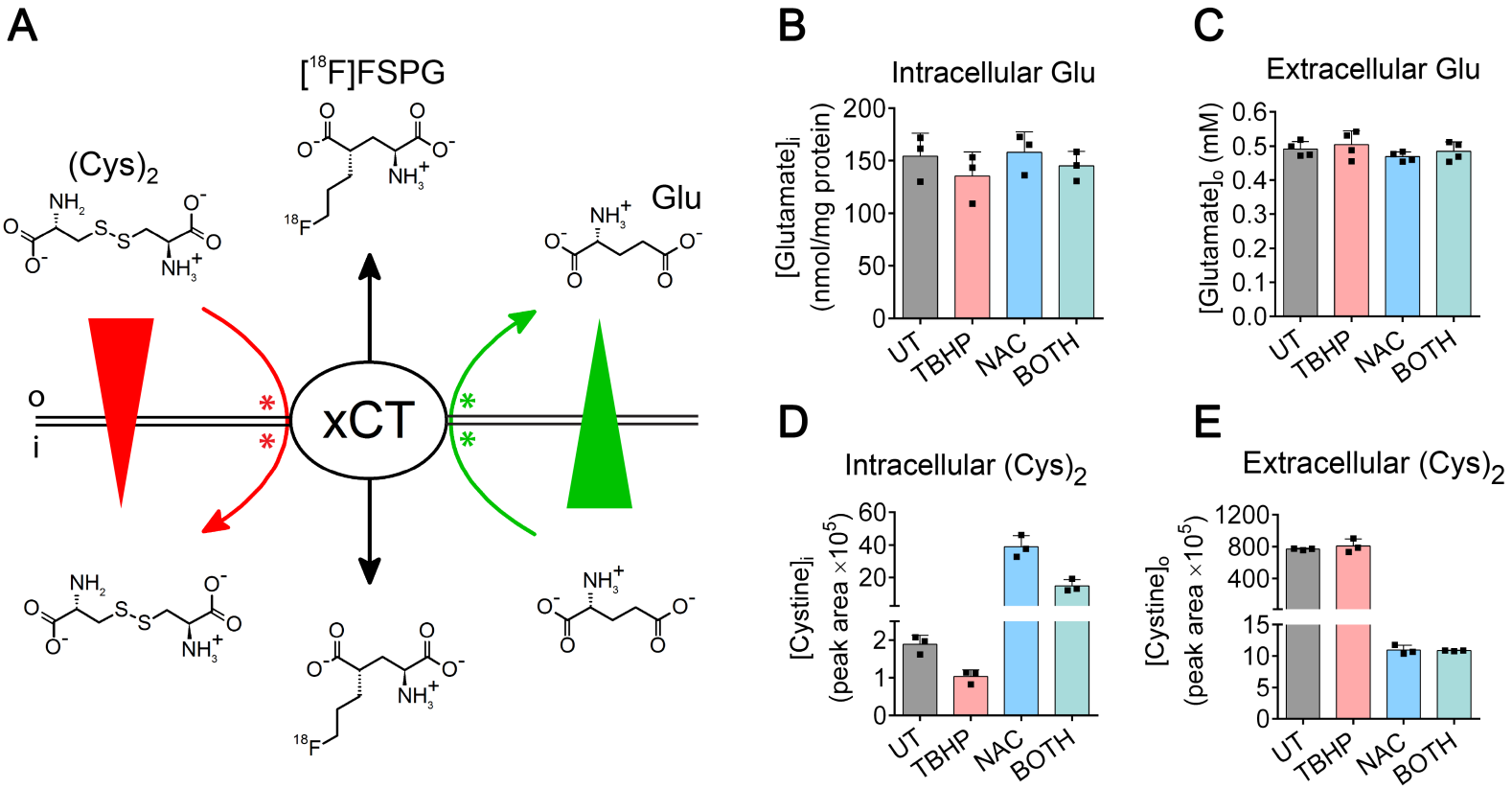
A
[18F]FSPG
(Cys)2
Glu
xCT
o
i
B
Intracellular Glu
[Glutamate]i (nmol/mg protein)
200
150
100
50
0
UT
TBHP
NAC
BOTH
C
Extracellular Glu
[Glutamate]o (mM)
0.6
0.5
0.4
0.3
0.2
0.1
0.0
UT
TBHP
NAC
BOTH
D
Intracellular (Cys)2
[Cystine]i (peak area ×10^5)
60
40
20
2
1
0
UT
TBHP
NAC
BOTH
E
Extracellular (Cys)2
[Cystine]o (peak area ×10^5)
1200
800
400
15
10
5
0
UT
TBHP
NAC
BOTH

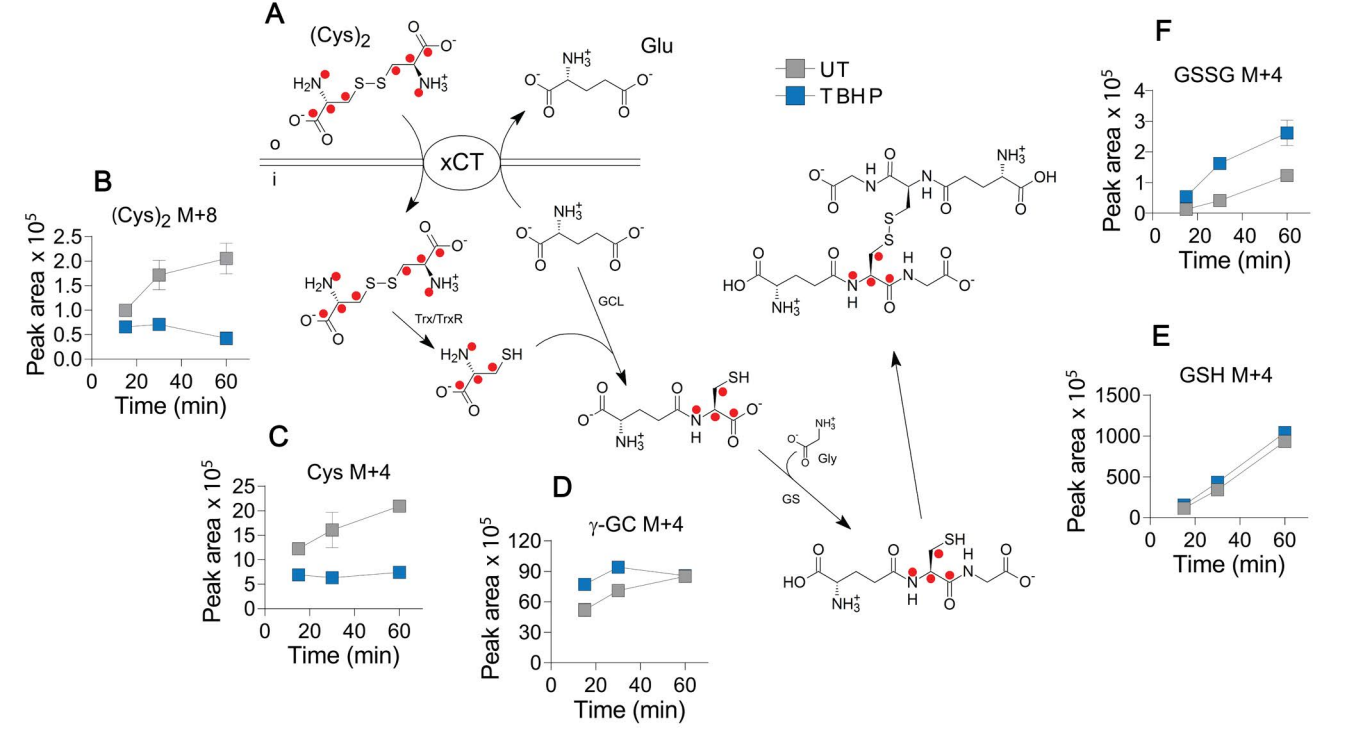
A
(Cys)2
Glu
o
i
xCT
GCL
Trx/TrxR
Gly
GS
UT
TBHP
B
(Cys)2 M+8
Peak area x 10^5
Time (min)
C
Cys M+4
D
γ-GC M+4
E
GSH M+4
F
GSSG M+4

FIGURE 5

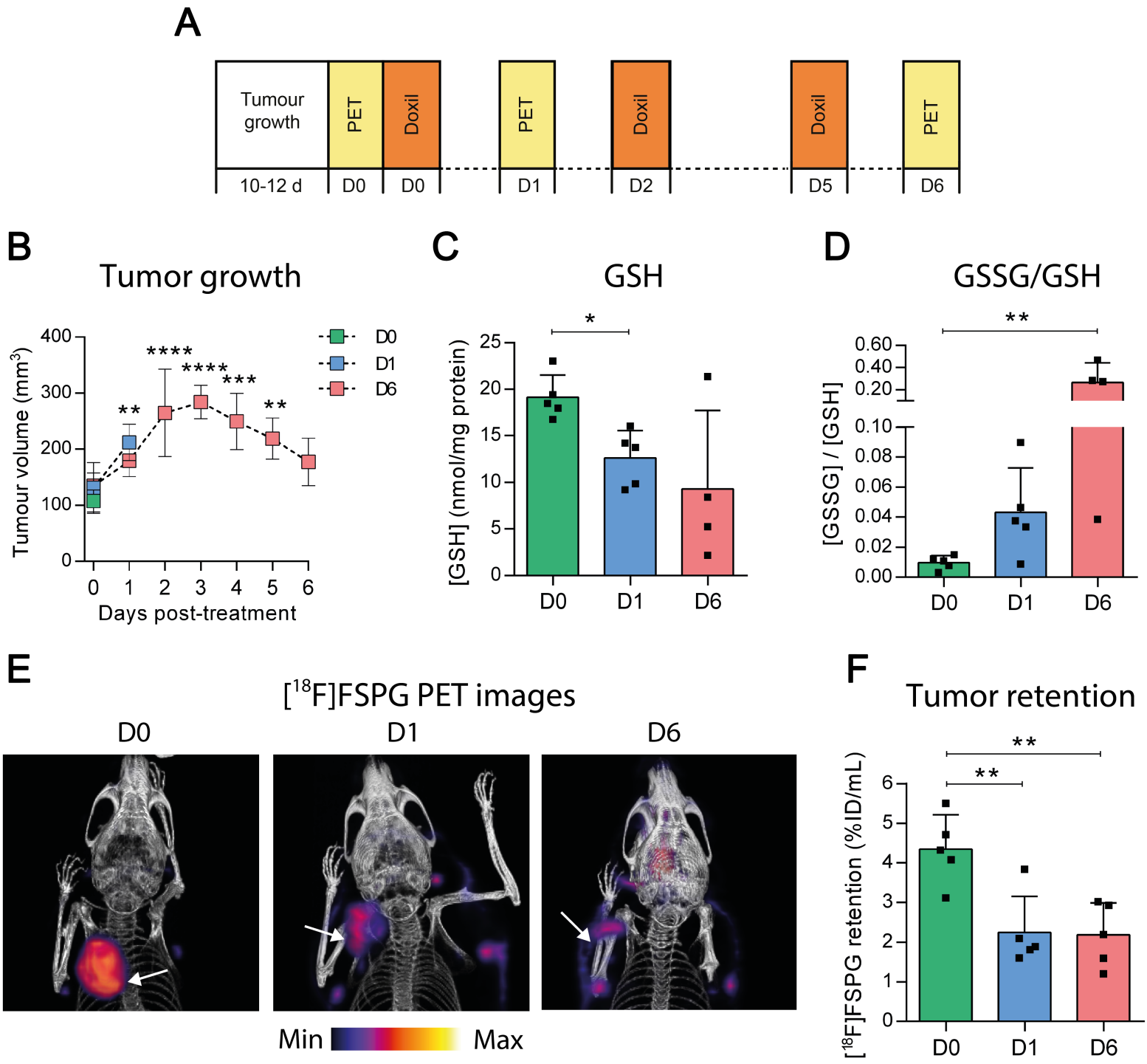
A
Tumour growth
PET
Doxil
PET
Doxil
Doxil
PET
10-12 d
D0
D0
D1
D2
D5
D6
B
Tumor growth
Tumour volume (mm3)
Days post-treatment
D0
D1
D6
C
GSH
[GSH] (nmol/mg protein)
D
GSSG/GSH
[GSSG] / [GSH]
E
[18F]FSPG PET images
D0
D1
D6
Min
Max
F
Tumor retention
[18F]FSPG retention (%ID/mL)